

# Quantum spill-out in nanometer-thin gold slabs: Effect on the plasmon mode index and the plasmonic absorption

Enok J. H. Skjølstrup,<sup>\*</sup> Thomas Søndergaard, and Thomas G. Pedersen

*Department of Materials and Production, Aalborg University, Skjernvej 4A, DK-9220 Aalborg East, Denmark*



(Received 12 October 2018; published 26 April 2019; corrected 26 April 2019)

A quantum mechanical approach and local response theory are applied to study plasmons propagating in nanometer-thin gold slabs sandwiched between different dielectrics. The metal slab supports two different kinds of modes, classified as long- and short-range plasmons. Quantum spill-out is found to significantly increase the imaginary part of their mode indices, and, surprisingly, even for slabs wide enough to approach bulk the increase is 20%. This is explained in terms of enhanced plasmonic absorption, which mainly takes place in narrow regions located near the slab surface.

DOI: [10.1103/PhysRevB.99.155427](https://doi.org/10.1103/PhysRevB.99.155427)

## I. INTRODUCTION

Recently, it was found that the effect of quantum spill-out in nanometer-thin gaps in gold has a significant impact on the propagation of surface plasmon polaritons (SPPs) in such structures. In the limit of vanishing gap, the SPP mode index was found to converge to the refractive index of bulk gold [1], while classical models neglecting spill-out find a diverging mode index [2,3]. In addition, it was discovered in Ref. [1] that spill-out significantly increases the plasmonic absorption in these gaps. Furthermore, the predicted reflectance from an ultrasharp groove array is in much better agreement with measurements [4] than the classical model [5,6].

In this paper, we study the opposite geometry, i.e., a nanometer-thin gold slab surrounded by different dielectrics. Such a structure supports long- and short-range SPPs, which are  $p$ -polarized electromagnetic waves bound to and propagating along the slab [7–11]. For a nanometer-thin slab, the short-range mode is strongly bound, meaning that a large part of the field profile is located in the slab region, while the long-range mode is weakly bound with most of its field profile located in the dielectric regions. The magnetic fields of the modes are symmetric and antisymmetric, respectively, if the metal slab is sandwiched between identical dielectrics, while the symmetry is broken when sandwiched between different dielectrics [9]. Applications of such SPPs are found in, e.g., plasmonic lenses for biosensors and as mode couplers into dielectric or plasmonic waveguides [12,13]. In addition, plasmonic structures find applications within, e.g., solar cells [14] and, furthermore, they can be applied to squeeze light below the diffraction limit [15,16], and can be utilized in lasers [17].

Plasmons supported by metal slabs have previously been studied using both classical and quantum models [7–11,18–21]. Thus, Refs. [7–11] applied a classical model neglecting quantum spill-out, such that the dielectric function takes one value in the metal region and another value in the

dielectric region, thus changing abruptly at the interfaces, while quantum effects have been included in, e.g., Refs. [18–21]. Furthermore, gold films with thicknesses down to 1 nm have recently been fabricated [22].

Here, we examine the effect of quantum spill-out on plasmons propagating in nanometer-thin gold slabs. Local response theory is applied to calculate the mode indices and associated electromagnetic fields. We show that spill-out significantly increases the imaginary part of the mode index, even for slabs wide enough to approach bulk. This is explained in terms of strong plasmonic absorption mainly taking place a few Å from the slab surface, a phenomenon not found in classical models.

## II. QUANTUM DIELECTRIC FUNCTION

In the vicinity of the gold slab, the electron density and the effective potential arising from the free electrons (in the  $s$ ,  $p$  band) are significantly modified due to electron tunneling through the surface barrier. To capture this effect, we calculate the electron density using density-functional theory (DFT) in the jellium model [23,24] (see Appendix A for further description). The optical cross sections of metal nanowires [25–28], metal clusters, and spheres [25,29–31] have previously been calculated by applying such a DFT model in the jellium approximation. Likewise the plasmon resonances of metal dimers and semiconductor nanocrystals have been calculated in Refs. [32–34], while Ref. [20] studied the plasmonic properties of ultrathin metal films. In addition, Ref. [35] examined the role of electron spill-out and nonlocal effects on the plasmon dispersion relation for gap plasmons propagating between two gold surfaces as well as plasmons propagating in gold slabs surrounded by air. It was found in that paper that spill-out has a significant impact while the influence from nonlocal effects was minor. In Refs. [20,35], only the real part of the parallel wave number (analogous to mode index) was considered, with no studies of the dependence of the slab (or gap) width on plasmon propagation. In this paper, in contrast, we compute both real and imaginary parts of the mode index

<sup>\*</sup>ejs@mp.aau.dk

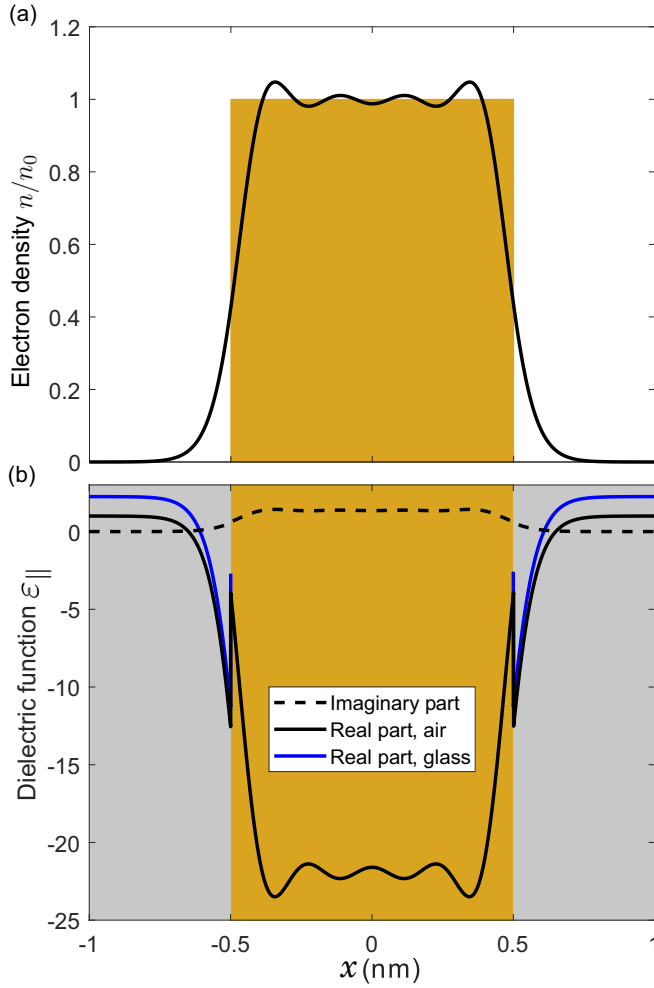


FIG. 1. (a) Electron density in units of the bulk gold density  $n_0$  across a gold slab of width 1 nm. (b) Real and imaginary parts of the dielectric function  $\epsilon$  across the same gold slab at a wavelength of 775 nm, with the shaded areas indicating the surrounding dielectrics. The solid black (blue) curve is for a slab surrounded by air (glass) on both sides. The imaginary part is unaffected by the kind of dielectric. In both figures, the colored areas represent the ion charge.

and, furthermore, investigate in detail how they depend on the slab width.

The electron density  $n$  across a gold slab of width  $d = 1$  nm is shown in Fig. 1(a) in units of the bulk gold density  $n_0$ , where the geometry is chosen such that the  $x$  axis is perpendicular to the slab, while the plasmons are propagating in the  $y$  direction. The colored area in the figure shows the position of the ion charge in the jellium model, and spill-out is clearly seen as the electron density contains an exponential tail that stretches  $\sim 0.3$  nm into the dielectric region. In addition, charge is conserved ( $\int n(x)dx = n_0d$ ), and the density inside the slab is thus also affected by spill-out. In Fig. 1(a) the integrated value of the spilled-out charge is  $0.05n_0d$ . As the slab gets wider, the electron density near the slab boundary contains Friedel oscillations in agreement with Refs. [23,24,36] where the electron density at a single interface between gold and air was studied.

The dielectric response function has been studied in several papers [37–43] using a fully quantum mechanical approach within the random phase approximation [44]. As the metal slab is a two-dimensional (2D) material, it only has boundaries in the direction perpendicular to the slab, implying that the response is anisotropic. The tensorial dielectric function  $\overleftrightarrow{\epsilon}(x, x')$  can be obtained from the electric conductivity in Ref. [43] as

$$\begin{aligned} \overleftrightarrow{\epsilon}(x, x') = & \left( 1 - \frac{e^2 n(x)}{m_e \epsilon_0 (\omega^2 + i\Gamma\omega)} \right) \delta(x - x') \overleftrightarrow{I} \\ & - \frac{1}{2\pi^2 \epsilon_0 \hbar \omega^2} \sum_{n,m} \int f_{nm}(\vec{k}_{\parallel}) \\ & \times \frac{\vec{j}_{nm}(\vec{k}_{\parallel}, x) \vec{j}_{mn}(\vec{k}_{\parallel}, x')}{\omega + i\Gamma + \omega_m - \omega_n} d^2 k_{\parallel}. \end{aligned} \quad (1)$$

Here, the first line is a local isotropic Drude term, where the spatially varying electron density  $n(x)$  corresponds to a position-dependent plasma frequency  $\omega_p^2(x) = e^2 n(x)/(m_e \epsilon_0)$ , where  $e$  and  $m_e$  denote the electron charge and mass, respectively. In the second line of Eq. (1),  $f_{nm}(\vec{k}_{\parallel})$  denotes the difference between Fermi factors of states with energies  $\hbar\omega_n$  and  $\hbar\omega_m$ , respectively, where  $\vec{k}_{\parallel}$  is in the  $(y, z)$  plane, thus parallel to the slab. Furthermore,  $\vec{j}_{nm}$  is a matrix element of the transition current (see Appendix B for an explicit expression) and  $\Gamma$  is a damping term. The second line of Eq. (1) is denoted  $\overleftrightarrow{\epsilon}_{NL}(x, x')$ . Equation (1) shows, thus, that rigid quantum mechanical response theory implies a dielectric response function that is separable into a local isotropic and a nonlocal anisotropic term. The nonlocality has been studied in several papers [18,21,45–48], and for metal dimers and cylinders it is found to only slightly blue-shift the plasmon resonances, illustrating, as in Ref. [35], that nonlocality is a relatively small modification to the dielectric response.

For the short-range mode, the  $x$  and  $y$  components of the electric field are odd and even, respectively [7,8]. From the expressions of  $\vec{j}_{nm}$  in Appendix B this implies that the nonlocal part of the displacement field  $\vec{D}_{NL}(x) = \epsilon_0 \int \overleftrightarrow{\epsilon}_{NL}(x, x') \cdot \vec{E}(x') dx'$  is zero on average across the slab, where the contribution from the  $x$  component of the field is zero because the field is odd, while the contribution from the  $y$  component is zero due to orthogonality of the wave functions applied in  $\vec{j}_{nm}$ . For the  $y$  component the same applies for the long-range mode. Based on symmetry arguments, this explains the physics behind the small impact from the nonlocal effects on the short-range mode. The same phenomenon has previously been discussed for other cases in Refs. [18,21,35,45–48].

For the long-range mode, the  $x$  component of the field is almost constant across the slab [7,8], which implies that the contribution to  $\vec{D}_{NL}$ , which is nonzero on average, is reduced to an integral of the  $\hat{x}\hat{x}$  component of  $\overleftrightarrow{\epsilon}_{NL}$  with respect to  $x'$ . In this paper, the nonlocal part of the dielectric function is taken into account by an averaging procedure, which leads to an anisotropic step function that gives the correct net response from the slab for both kinds of modes. It is modeled as a piecewise constant function taking the value  $\iint \overleftrightarrow{\epsilon}_{NL} dx dx' / d$  inside the slab and zero outside (see Appendix B for details). The effect of spill-out is included

in the first line of Eq. (1), while the effects of interband transitions and dielectric substrates will be incorporated by modifying the local dielectric function as shown below.

In general, the dielectric tensor is given by  $\overleftrightarrow{\epsilon} = \text{diag}(\epsilon_{\perp}, \epsilon_{\parallel}, \epsilon_{\parallel})$  [49], where the parallel part  $\epsilon_{\parallel}$  is similar to the one in Ref. [1]. In the bulk, the electron density  $n_0$  implies a bulk plasma frequency of  $\omega_{p,\text{bulk}} = \sqrt{n_0 e^2 / (m_e \epsilon_0)}$ , which gives rise to a Drude response  $\epsilon_{p,\text{bulk}}(\omega) = 1 - \omega_{p,\text{bulk}}^2 / (\omega^2 + i\Gamma\omega)$  [50]. Bound electrons in the lower-lying  $d$  bands also contribute to the dielectric function [50], but in contrast to the free electrons, we assume, as in Ref. [35], that they are entirely located in the jellium region, thus not tunneling through the potential barrier. The response from the bound electrons is calculated from the experimental response of bulk gold  $\epsilon_{\text{gold}}(\omega)$  from Ref. [51] as  $\epsilon_{\text{bound}}(\omega) = \epsilon_{\text{gold}}(\omega) - \epsilon_{p,\text{bulk}}(\omega)$ . The parallel part of the final dielectric tensor in the vicinity of a gold slab with a jellium region spanning from  $x = -d/2$  to  $d/2$  is therefore given by

$$\epsilon_{\parallel}(\omega, x) = 1 - \frac{\omega_p^2(x)}{\omega^2 + i\Gamma\omega} + [\epsilon_s(x) - 1]\theta(|x| - d/2) + \epsilon_{\text{bound}}(\omega)\theta(d/2 - |x|). \quad (2)$$

Here, the first term describes the local Drude response of free electrons with position-dependent plasma frequency  $\omega_p(x) = \sqrt{n(x)e^2 / (m_e \epsilon_0)}$  determined by the electron density  $n(x)$  calculated using DFT. Also,  $\hbar\Gamma = 65.8$  meV has been applied for the damping term [50]. The dielectric substrate and superstrate, which in general can be different, are described by  $\epsilon_s(x)$ , and the Heaviside step function  $\theta$  in the first line makes sure that the dielectric function sufficiently far from the slab equals the correct values in the substrate and superstrate. Hence, it has been assumed that the electron density across the slab does not depend on the kind of substrate and superstrate it is surrounded by. Lastly, the abrupt behavior assumed for the bound electron term is modeled with the same step function  $\theta$  as used to describe the anisotropic response discussed above. The perpendicular part of the dielectric tensor is written as

$$\epsilon_{\perp}(\omega, x) = \epsilon_{\parallel}(\omega, x) + \epsilon_{\text{ani}}(\omega, d)\theta(d/2 - |x|), \quad (3)$$

where the expression for the anisotropic term  $\epsilon_{\text{ani}}(\omega, d)$  is given in Appendix B. Anisotropy has previously been included in Refs. [21,49] but neglected in several other papers [1,19,20,28–30].

An example of the parallel part of the dielectric function is seen in Fig. 1(b) for a slab width of 1 nm at a wavelength of 775 nm. For a gold slab placed on a glass substrate with air as superstrate, the blue curve to the left and the black curve to the right of the slab describe the dielectric function in the glass and air, respectively. The real part of the dielectric function is clearly seen to jump at the slab boundary due to the step function in the second line of Eq. (2). Although it is difficult to see in the figure, the imaginary part of the dielectric function also jumps across the interfaces. Since the substrate and superstrate are assumed lossless, the imaginary part of the dielectric function is unaffected by these materials.

### III. MODE INDEX OF PROPAGATING PLASMONS

The magnetic field of the SPPs only has a  $z$  component and is given by [6]

$$\vec{H}_m(\vec{r}) = \hat{z}H_m(x, y) = \hat{z} \exp(ik_0\beta_m y)H_m(x), \quad (4)$$

where the subscripts  $m = \{l, s\}$  indicate that the field and associated complex mode index  $\beta$  can be either long range or short range, respectively, in agreement with Ref. [9]. In Eq. (4),  $k_0 = 2\pi/\lambda$  is the free-space wave number, and  $H_m(x)$  is the transverse magnetic field distribution. Both the mode index and the transverse magnetic field depend strongly on  $d$ , especially for the short-range mode, as will be shown below.

The plasmon mode indices are found as poles in the reflection coefficient [50,52], which is calculated by a transfer matrix method relating the magnetic fields to the left and right of the structure [1] (see Appendix B for the incorporation of anisotropy and Appendix C for classification of modes).

Figures 2 and 3 show, respectively, the short- and long-range mode indices as a function of  $d$  at a wavelength of 775 nm, where the response is isotropic in Fig. 2. For the blue and red curves in Fig. 2(a), the geometric structure is symmetric, while it is asymmetric for the green curves in Fig. 2(b), as indicated in the text above each subfigure. This implies that the magnetic fields associated with the blue and red curves are antisymmetric, while the symmetry of the associated fields is broken for the corresponding green curves, which will be demonstrated in the next section.

It is found that the relative effect of anisotropy on both components of the short-range mode indices is small, why Fig. 2 only shows the mode indices for an isotropic response. Mode indices calculated with an anisotropic response are instead shown for the long-range mode in Fig. 3. The results in Fig. 2 are in agreement with previous studies [7–9] when spill-out is neglected. The real parts are almost unaffected by spill-out, while it plays a significant role for the imaginary parts, as will be elaborated upon below. A similar calculation of the mode index with and without spill-out for gap plasmons propagating in narrow gaps in gold showed that the mode index when including spill-out converges to the refractive index of bulk gold in the limit of vanishing gap width [1], while neglecting spill-out leads to an unphysically diverging mode index [2,3]. For plasmons bound to the slab, the mode index when neglecting spill-out also diverges unphysically in the limit of vanishing slab thickness [7–9]. This is not the case with spill-out included, as plasmonic modes only exist when the real part of the metal dielectric constant is negative in some region along the direction normal to the slab [50]. It is found that for a slab of subatom thickness ( $\sim 0.3$  Å), the electron density becomes so delocalized that the real part of the dielectric constant is everywhere positive. Hence, with spill-out included, the mode index does not diverge in the limit of vanishing slab thickness. Instead, plasmonic modes cease to exist for slabs below a cutoff thickness in the subatom range. However, since a gold atom has a diameter of roughly 0.3 nm [4], we only consider slab widths larger than this value.

For an asymmetric structure with glass as substrate and air as superstrate, the short-range mode index is shown in Fig. 2(b). Here, it is difficult to see the difference in mode

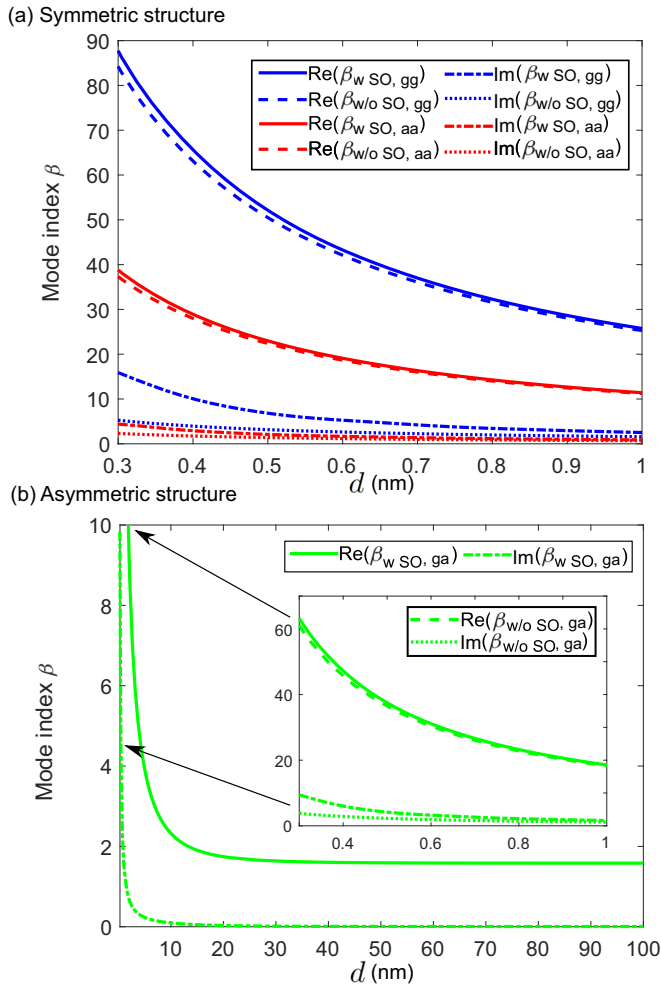


FIG. 2. Real (solid and dashed lines) and imaginary (dotted and dashed-dotted lines) parts of the short-range mode index vs slab width  $d$  at a wavelength of 775 nm. Results are shown for spill-out (SO) included (solid and dashed-dotted lines) and neglected (dashed and dotted lines). In (a) the structure is symmetric, and the blue and red lines are for slabs surrounded by glass (gg) and air (aa), respectively. In (b) the structure is asymmetric, where the slab is surrounded by glass and air (ga), and the inset shows a zoom for  $d$  below 1 nm. In both (a) and (b), the response is isotropic.

index with and without spill-out when the slab width exceeds 1 nm. Therefore, the mode index when neglecting spill-out is only included in the inset showing results for  $d$  below 1 nm, where  $\beta$  has the same behavior as for the symmetric structure in Fig. 2(a). Although it is hard to see in the figure, the imaginary part is small but nonzero for all slab widths. The mode index has converged when  $d = 100$  nm, and for such a wide slab the plasmon behaves as if bound to a single interface between glass and gold [50].

The asymmetric structure also supports long-range modes, but only for slab thicknesses above a certain threshold [8]. The long-range mode is mainly bound to the air-gold interface, with a mode index that is lower than the refractive index of the glass substrate. This implies that the normal component of the wave vector becomes real (with a very small imaginary part due to loss in the gold) on the glass side of the structure,

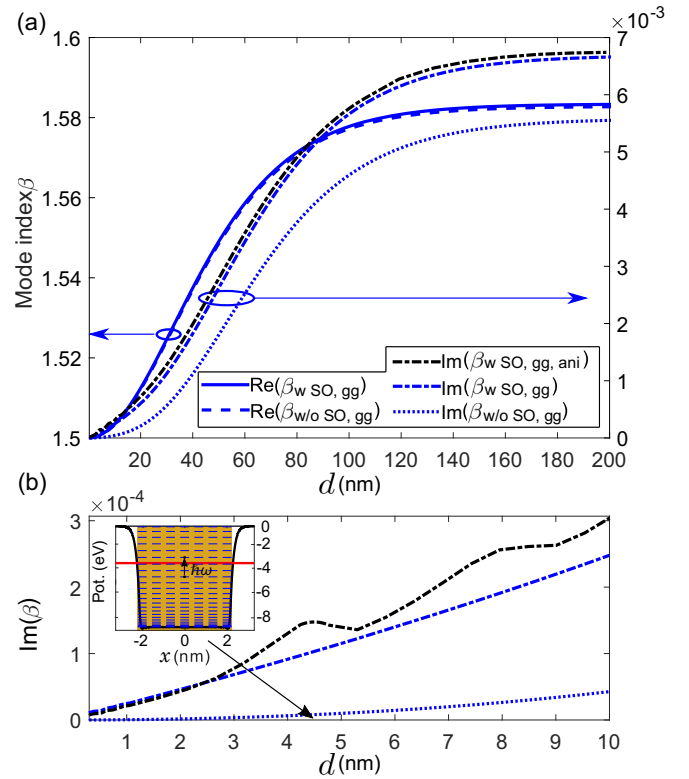


FIG. 3. Long-range mode index for a slab surrounded by glass (gg) at a wavelength of 775 nm. In (a), the real and imaginary parts are shown on the left and right y axes, respectively, as indicated by the arrows. The black dashed-dotted line shows the imaginary part of the mode index when the response is anisotropic. (b) Shows a zoom of the imaginary part in (a) for  $d$  below 10 nm, where the line types have the same meaning as in (a). Inset shows the potential barrier for a slab of width 4.5 nm, as indicated by the arrow, where the Fermi energy is shown by the red horizontal line, and all the discrete quantum energy levels as the dashed blue horizontal lines. A transition between an occupied and an empty state with energy difference  $\hbar\omega$  is illustrated by the vertical arrow, and is near resonance at the wavelength of 775 nm.

leading to a wave propagating in the substrate, thus not a truly bound mode [10]. Hence, the wave will leak out into the substrate, where conservation of momentum determines the leakage angle [52]. However, if the dielectric constants of the substrate and superstrate are not too different, it is possible to obtain a long-range mode that is truly bound to both interfaces (see, e.g., Fig. 3 in Ref. [9]). The phenomenon of leaky modes can be examined using leakage radiation microscopy (see, e.g., Refs. [10,53,54]).

Figure 3(a) shows the mode index of the corresponding long-range mode for a gold slab surrounded by glass, where the response is isotropic for the blue lines and anisotropic for the black line. Again, the results are in agreement with previous studies [7–9] when spill-out is neglected. In this case, the mode index for an ultrathin slab is very close to the refractive index of the substrate, which implies that the mode is weakly bound. The mode is therefore long range with most of its field profile located in the dielectric regions, which will be illustrated in the next section. As the slab width

increases to 200 nm, the mode index without spill-out has converged to  $\sqrt{\epsilon_{\text{gold}}\epsilon_{\text{glass}}}/(\epsilon_{\text{gold}} + \epsilon_{\text{glass}})$ , which is the mode index of a plasmon bound to a single interface between gold and glass [50]. In addition, the corresponding short-range mode index when neglecting spill-out in Fig. 2(a) converges to the same value for  $d = 200$  nm (not shown) in agreement with Refs. [8,9,12]. With spill-out included, the long-range mode index for small slabs in Fig. 3(a) is also close to the refractive index of the substrate, and the imaginary part is very low. As for the short-range mode in Figs. 2(a) and 2(b), especially the real part of the mode index is almost the same with and without spill-out, as seen by comparing the solid and dashed lines. But, importantly, spill-out significantly increases the imaginary part of the mode index, even for slab widths up to 200 nm, as seen by comparing the dotted and dashed-dotted lines in Fig. 3(a). When including anisotropy in the model, it is found that the real part of the mode index is almost unchanged (not shown), while the imaginary part is modified. For wide slabs the effect of anisotropy is small, in agreement with Ref. [49], as can be seen by comparing the blue and black dashed-dotted lines. The same small effect of anisotropy for wide slabs is found for the short-range mode in Fig. 2(a) (not shown). In the other limit when the slab width is only a few nm, the imaginary part of the long-range mode index is modified due to anisotropy, as seen in Fig. 3(b) showing a zoom of the imaginary parts in Fig. 3(a) for  $d$  below 10 nm. As these values are on the order of  $10^{-4}$ , this mode is relatively much more sensitive to anisotropy than the corresponding short-range mode in Fig. 2, even though the absolute change due to anisotropy is comparable for the two modes. The anisotropic part contains peaks corresponding to certain resonances in electronic transitions (see Appendix B for details). For a wavelength of 775 nm, a resonance is found at a slab width of 4.5 nm, for which the potential barrier is shown in the inset, where the zero in potential is chosen to be sufficiently far from the slab. A transition between an occupied and an empty state with energy difference  $\hbar\omega$  is illustrated by the vertical arrow. For wider slabs, the individual energy levels are closer, and become continuous in the bulk limit, implying that the response tends to become isotropic in this limit.

Having now briefly accounted for the relative small impact of anisotropy, we turn to further illustrate the effect of spill-out in a symmetric structure. Hence, in the remaining part of the paper, the shown results are all obtained using an isotropic response. The ratio between mode indices with and without spill-out is shown in Figs. 4(a) and 4(b) for the short- and long-range modes, respectively. For both kinds of modes, the real part of the mode index is almost unaffected by spill-out, as the ratios shown by the solid lines in Fig. 4 have converged to 1.0004 when  $d = 50$  nm. For the short-range mode the ratio between the imaginary parts is approximately 3.0 for a slab width of 0.3 nm, while it converges to  $\sim 1.2$  for  $d = 200$  nm. The real part of the normalized magnetic field profile when spill-out is included is shown in the inset of Fig. 4(a) for a slab width of 200 nm, as indicated by the arrow. It behaves as two decoupled plasmons bound to the interfaces between glass and gold, as the field profiles bound to the individual interfaces do not interact for such a wide slab.

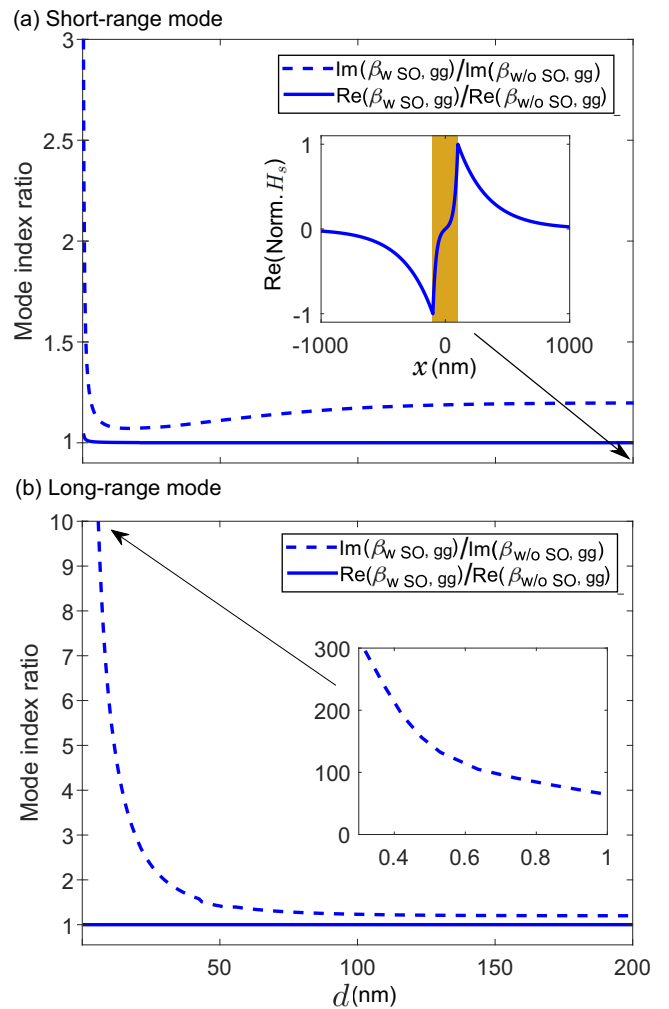


FIG. 4. Ratio between mode indices with and without spill-out at a wavelength of 775 nm for a slab surrounded by glass (gg). In (a), the mode is short range, and the inset shows the real part of the transverse magnetic field for  $d = 200$  nm, as indicated by the arrow, where the colored area represents the ion charge. In (b), the mode is long range and the inset shows a zoom for  $d$  below 1 nm. The response is isotropic.

For the long-range mode, the corresponding ratio between the imaginary parts is extremely high for small  $d$  as seen in the inset in Fig. 4(b). However, as  $d$  increases, the ratio decreases monotonically and converges to  $\sim 1.2$  when  $d = 200$  nm. This is an important result showing that quantum spill-out increases the imaginary part of the mode index by 20%, even for relatively thick slabs that can readily be fabricated [12,53] and approach bulk gold. It is highly surprising that spill-out plays such a significant role for wide slabs, as it only modifies the electron density in a region very close to the ion charge. In addition, it is noticed that the ratios between the imaginary parts of the two modes converge to the same value when the slab is wide enough, as in this case the field profiles bound to the individual interfaces are decoupled, similarly to classical models [8,9,12]. Furthermore, the short-range mode indices with and without spill-out in the asymmetric structure in Fig. 2(b) converge to the same values as for

the long-range mode in Fig. 3(a), as both modes behave as bound to a single interface between gold and glass. Hence, spill-out also increases the imaginary part of the mode index by 20% in an asymmetric structure. The physical meaning of the enhanced imaginary part is that the plasmon propagation length will be significantly shorter, while the unaltered real part implies that the propagation velocity will be unchanged.

Reference [20] applied an isotropic dielectric function with components analogous to Eq. (2) to study the effect of spill-out on plasmons propagating in a magnesium slab ( $r_s = 2.66$  bohrs) surrounded by silicon and air. With the present method, the real part of the calculated mode index agrees well with values estimated from Fig. 5 in Ref. [20], showing quantitative agreement between that paper and the method presented here. Likewise, the mode index calculated in this paper agrees well with values estimated from Figs. 6 and S9 in Ref. [35] regarding plasmons propagating in gold slabs surrounded by air.

#### IV. FIELD PROFILE AND PLASMONIC ABSORPTION

Once the mode indices have been computed, the magnetic field from Eq. (4) is calculated using the same transfer matrix method as described in Refs. [1,55]. In the last part of Appendix B it is shown how the method is slightly modified to describe the anisotropy. Applying the same phase convention as in Ref. [7], the normalized real part of the short-range transverse magnetic field  $H_s(x)$  across a gold slab of 0.3 nm is shown in Fig. 5(a) at a wavelength of 775 nm. The associated imaginary parts of the fields are not shown as they are small compared to the real parts, similarly to classical models [7].

When neglecting spill-out, the slope of the magnetic field, corresponding to the normal component of the electric field, becomes discontinuous across the slab surfaces in agreement with Refs. [7–9]. With spill-out included, the slope is still discontinuous due to the abrupt change in the bound electron term in Eq. (2), although it is difficult to see in Fig. 5(a). But, in the vicinity of the slab surface, the field profiles behave more smoothly, and their maximum positions are slightly shifted into the dielectric region. We have checked that the appropriate boundary conditions regarding electromagnetic fields across an interface [50] are satisfied. Further away from the slab, the field profiles with and without spill-out become almost identical. Consequently, the decay lengths into the dielectrics, calculated as  $1/\text{Im}(k_x)$ , where  $k_x = k_0\sqrt{\epsilon_s - \beta^2}$  is the wave number in the  $x$  direction, are very similar and both are on the order of a few nm. This illustrates that the short-range mode is strongly bound to the slab, as it decays very rapidly into the dielectrics [9], and thereby has a large part of its field profile located in the slab region. Notice that as the real part of the mode index is much higher than its imaginary part, the decay length mostly depends on the real part of the mode index. Figure 5(a) demonstrates that the short-range magnetic field is antisymmetric for the two symmetric structures shown by the blue and red curves, while this is no longer the case for an asymmetric structure, as shown by the green curves. When the slab width increases, the field profile broadens, as shown in the inset of Fig. 4(a) for a 200-nm-wide slab. For such a wide slab, the field profiles with

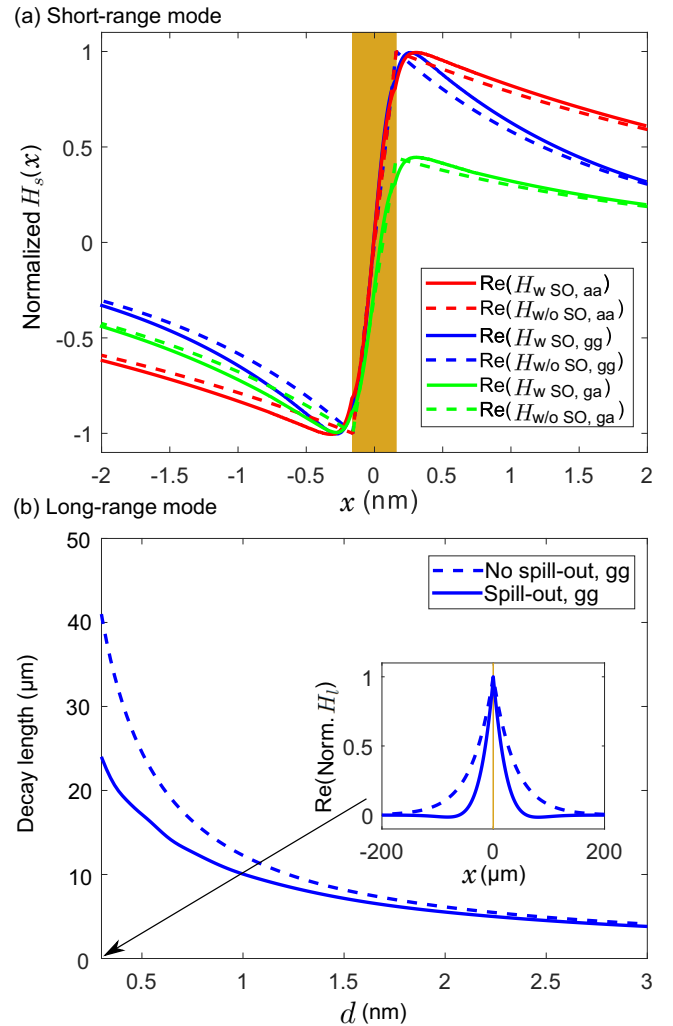


FIG. 5. (a) Normalized real part of  $H_s(x)$  across a slab of width 0.3 nm. (b) Shows the decay length of the long-range mode for a gold slab surrounded by glass (gg) with and without spill-out. The inset shows the real part of the magnetic field profiles for a slab of width 0.3 nm as indicated by the arrow. In both (a) and (b), the colored areas represent the ion charge, the wavelength is 775 nm, and the response is isotropic.

and without spill-out are almost identical, and both behave as two decoupled plasmons bound to the interfaces between glass and gold. When including anisotropy, the short-range mode indices were almost unchanged. This also applies for the magnetic fields, why Fig. 5(a) only shows the fields for an isotropic response.

As mentioned above, the long-range mode is weakly bound. Consequently, the electromagnetic fields for a few-nm slab have decay lengths of several micrometers, as shown for a gold slab surrounded by glass in Fig. 5(b). As the decay length mostly depends on the real part of the mode index, the decay length in Fig. 5(b) is in practice unchanged when the response is anisotropic. The long decay length implies that most of the field profiles are located in the dielectric regions. The field profiles are broader when spill-out is neglected, as also seen in the inset showing the real part of the magnetic fields across a slab of width 0.3 nm, i.e., the same slab as in

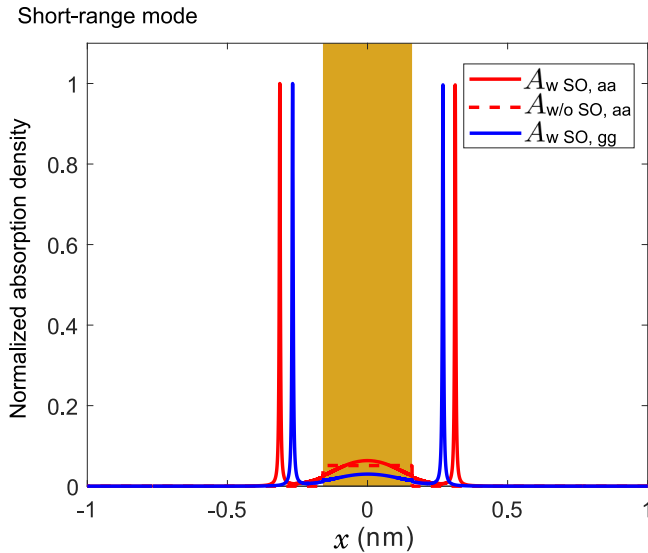


FIG. 6. Normalized absorption density for the short-range mode across a gold slab of width 0.3 nm at a wavelength of 775 nm. The solid and dashed lines show the absorption density when spill-out is included and neglected, respectively, where the red and blue lines are for slabs surrounded by air (aa) and glass (gg), respectively. The response is isotropic.

Fig. 5(a). Including spill-out effectively implies a broader slab [see Fig. 1(a)], which means that the fields become slightly more localized with a shorter decay length. For slabs wider than 3 nm, the decay lengths with and without spill-out are very similar, and both converge to the decay length of a plasmon bound to a single interface between gold and glass (not shown).

As argued above, spill-out plays almost no role for the decay length for slabs of a few nm. On the other hand, it significantly increases the imaginary part of the mode index as shown in Fig. 4. This leads us to investigate how spill-out affects the electric field and plasmonic absorption across the slab. First, the electric field is calculated from the magnetic field in Eq. (4) as [50]

$$\vec{E}_m(x, y) = \frac{i \overleftrightarrow{\epsilon}^{-1}(x, y) \vec{\nabla} \times [\hat{z} H_m(x, y)]}{\omega \epsilon_0}. \quad (5)$$

The electric field is subsequently used to calculate the absorption density defined as

$$A_m(x, y) = \text{Im}(\vec{E}_m^*(x, y) \cdot \overleftrightarrow{\epsilon}(x, y) \cdot \vec{E}_m(x, y)). \quad (6)$$

By considering the time average of the Poynting vector,  $\langle \vec{S} \rangle = 1/2 \text{Re}(\vec{E} \times \vec{H}^*)$  [50], it can be shown that conservation of energy implies that the plasmonic absorption and the imaginary part of the mode index are related in the following way:

$$\text{Im}(\beta) = \frac{c \epsilon_0 \int A_m(x, y) dx}{2 \int \text{Re}(\vec{E}_m(x, y) \times \vec{H}_m^*(x, y)) \cdot \hat{y} dx}. \quad (7)$$

We have checked that this relation is satisfied for both kinds of modes with and without spill-out. The normalized absorption density is shown in Fig. 6 for the short-range mode across the slab of width 0.3 nm at a wavelength of 775 nm. If spill-out

is neglected, absorption can only take place in the gold as the surrounding dielectrics are assumed lossless. In this case, the absorption density is almost unaffected by the kind of surrounding dielectric, why Fig. 6 only shows it for a slab surrounded by air. But, with spill-out included, strong plasmonic absorption occurs, and the absorption density mostly consists of two narrow peaks located in the dielectric regions close to the interfaces. At these positions, similarly to Refs. [1,56], the real part of the dielectric function is zero (at the wavelength 775 nm), while its imaginary part is small but nonzero, which ensures that the peaks in the absorption density are finite. The narrow peaks are found a few Å outside the ion charge, and the same is found for the long-range mode (not shown). The contribution from these peaks leads to enhanced plasmonic absorption, as they are a consequence of electron spill-out, and therefore not found in classical models. The peaks correspond to the increase in imaginary part of the mode index observed in Sec. III. For a slab surrounded by glass, the peaks occur slightly closer to the slab, as the real part of the dielectric function has its zero shifted slightly compared to the case with a slab surrounded by air [see Fig. 1(b)]. The same phenomenon was found in Ref. [20] for a magnesium slab surrounded by silicon and air. The peaks in absorption density due to spill-out were recently discussed in Ref. [1], where they were found to significantly reduce the reflectance from an ultrasharp groove array in much better agreement with measurements [4] compared to classical models [5,6]. Like for the magnetic field, the absorption density is almost unaffected by anisotropy, why Fig. 6 only shows results for an isotropic response.

The increased absorption loss due to spill-out will manifest itself as decreased propagation lengths in fabricated plasmonic structures. Losses in such structures have been studied in, e.g., Refs. [57–60], where it was found that the measured propagation length of plasmons propagating in a 70-nm silver film deposited on glass is significantly shorter than the one calculated using classical models [59,60]. In addition, attenuated total reflectance (ATR) has been studied for a silver film on glass in the Kretschmann configuration. It is found that the measured reflectance at the Kretschmann angle [50] is significantly lower than the one calculated using classical models [61,62], illustrating that the losses are higher than expected from a classical point of view. Hence, these works together with Ref. [1] also support the finding that a classical model is not sufficient to correctly describe losses occurring in plasmonic waveguides.

## V. CONCLUSION

In conclusion, we have applied a quantum mechanical approach and local response theory to study the propagation of plasmons in nanometer-thin gold slabs surrounded by different dielectrics. The effect of spill-out is found to be small on the real part of the mode indices but remarkably increases the corresponding imaginary part, and even for slabs wide enough to approach bulk the increase is 20%. This is explained in terms of enhanced plasmonic absorption mainly taking place in narrow regions located a few Å outside the ion charge. It is highly surprising that spill-out plays such a significant role for wide slabs, as it only modifies the electron density in a region

very close to the ion charge. For slab widths above a few nanometers, the decay length of the fields into the dielectrics is almost unaffected by spill-out, as it mostly depends on the real part of the mode index. By taking anisotropy into account, a comparable change is found in the imaginary part of the mode index for both kinds of modes, while the relative change, however, is much larger for the long-range mode. When the slab width increases, the effect of anisotropy becomes less pronounced, and for a 200-nm-wide slab the response is almost isotropic. Furthermore, in contrast to classical models, the short-range mode index does not diverge in the limit of vanishing slab thickness when spill-out is included. Instead, plasmonic modes cease to exist for slab widths below a cutoff thickness in the subatom region.

### ACKNOWLEDGMENT

This work was supported by the QUSCOPE center sponsored by the Villum Foundation.

### APPENDIX A: CALCULATION OF ELECTRON DENSITY

In this Appendix, we discuss in more detail how the electron density is calculated. Within the jellium model it is assumed that the charge of the gold ions is smeared out, such that their charge density is constant within the slab [23,24]. The characteristic spill-out, as seen in Fig. 1(a), stems from the distribution of free electrons in the vicinity of this positive background. The Kohn-Sham equations [23] are solved self-consistently within the local density approximation (LDA) [44], applying the Perdew-Zunger parametrization [63] for the correlation term. The applied Wigner-Seitz radius for gold is  $r_s = 3.01$  bohrs [24].

It is found that 2500 basis functions on the form  $\sin(m\pi(x/L + 1/2))$  are sufficient to describe the density for slab widths up to 200 nm. The length  $L$  is 1 nm larger than the slab width  $d$ , and the slab is centered at  $x = 0$ . As in Ref. [1], the density is said to converge when a variation in Fermi energy between two iterations below  $10^{-7}$  Ha is achieved. Furthermore, in the Anderson mixing scheme [64], the mixing parameter  $\alpha$  must be below a certain threshold which strongly decreases with  $d$ . It is found that  $\alpha \leq 5 \times 10^{-4}$  is necessary for slab thicknesses up to 20 nm. The potentials for wider slabs can afterward be constructed from the potential of the 20-nm slab, as the oscillations in potential near its center are negligible, meaning that the effective potential near the center can be seen as constant. This constant potential is added in the central region of wider slabs.

### APPENDIX B: ANISOTROPY

In this Appendix, we discuss how the anisotropic term  $\varepsilon_{\text{ani}}(\omega, d)$  in Eq. (3) is calculated, and how the transfer matrix method is slightly modified to describe an anisotropic response. As mentioned in Sec. II, we approximate the nonlocal part of the dielectric tensor by a piecewise constant function taking the value  $\iint \overleftrightarrow{\varepsilon}_{NL}(x, x') dx dx' / d$  inside the slab and zero outside. From Ref. [43], the transition matrix elements

used in Eq. (1) are given by

$$\vec{j}_{nm}(\vec{k}_{\parallel}, x) = -\frac{e\hbar}{2m_e i} (2i\vec{k}_{\parallel} A_{nm}(x) + \hat{x} B_{nm}(x)), \quad (\text{B1})$$

where

$$\begin{aligned} A_{nm}(x) &= \varphi_n(x) \varphi_m^*(x), \\ B_{nm}(x) &= \varphi_m^*(x) \frac{\partial \varphi_n(x)}{\partial x} - \varphi_n(x) \frac{\partial \varphi_m^*(x)}{\partial x}. \end{aligned} \quad (\text{B2})$$

Here, the  $\varphi_n$ 's are the wave functions corresponding to the energies  $E_n = \hbar\omega_n$  in Eq. (1). From Eqs. (B1) and (B2), the parallel part of the step function is found to be zero due to the orthogonality of the wave functions. Using the commutator relation  $\langle \varphi_m | \hat{p}_x | \varphi_n \rangle = im_e E_{mn} \langle \varphi_m | x | \varphi_n \rangle / \hbar$ , where  $E_{mn} = E_m - E_n$ , and the oscillator strength  $g_{mn} = 2m_e |\langle \varphi_m | x | \varphi_n \rangle|^2 E_{mn} / \hbar^2$ , the perpendicular part describing the anisotropy can be shown to be

$$\begin{aligned} \varepsilon_{\text{ani}}(\omega, d) &= \frac{e^2}{\pi d \varepsilon_0 \hbar^2 (\omega + i\Gamma)^2} \\ &\times \sum_{m,n} g_{mn} \frac{E_{mn}^2 (E_F - E_n) \theta(E_F - E_n)}{E_{mn}^2 - \hbar^2 (\omega + i\Gamma)^2}. \end{aligned} \quad (\text{B3})$$

Here, the energies and number of bands depend strongly on  $d$ . A resonance is found when  $E_{mn}$  for a certain transition is close to the photon energy  $\hbar\omega$ , as illustrated by the vertical arrow in the inset of Fig. 3(b). When the slab width increases to 200 nm, the anisotropic term tends to zero, implying that the response becomes isotropic in this limit.

When describing anisotropy, the reflection and transmission coefficients in the transfer matrix method are slightly modified into [65]

$$r_{ij} = \frac{k_{x,i} \varepsilon_{\parallel,j} - k_{x,j} \varepsilon_{\parallel,i}}{k_{x,i} \varepsilon_{\parallel,j} + k_{x,j} \varepsilon_{\parallel,i}}, \quad t_{ij} = 1 + r_{ij}, \quad (\text{B4})$$

where  $k_{x,i} = k_0 \sqrt{\varepsilon_{\parallel,i} - \beta^2 \varepsilon_{\parallel,i} / \varepsilon_{\perp,i}}$ . It is seen that if the material is isotropic,  $\varepsilon_{\parallel,i} = \varepsilon_{\perp,i}$ , the original coefficients from Ref. [55] are restored.

### APPENDIX C: CLASSIFICATION OF PLASMONIC MODES

In this short Appendix, we discuss how the plasmonic modes are classified. The mode index is calculated by the same type of transfer matrix method as presented in detail in Ref. [1]. However, only one kind of plasmonic mode was studied in that paper, while the classification of modes was not presented there. A structure matrix  $\mathcal{S}$  is constructed, which relates the magnetic fields to the left and right of the structure, and a mode index is found when the matrix element  $\mathcal{S}_{11}$  is zero, as this condition yields a pole in the reflection coefficient. The mode is classified by the sign of  $\mathcal{S}_{21}$ , where positive and negative signs correspond to long- and short-range modes, respectively, and  $\mathcal{S}_{21}$  is exactly  $\pm 1$  for symmetric structures. Expressions for the matrix elements can be found in Refs. [1,55]. In addition, the  $x$  axis is divided into tiny segments, each modeled as having a constant dielectric function. Similarly to Ref. [1], we find that segments of  $2.7 \times 10^{-4}$  nm are sufficient to avoid discretization errors.

- [1] E. J. H. Skjølstrup, T. Søndergaard, and T. G. Pedersen, *Phys. Rev. B* **97**, 115429 (2018).
- [2] F. J. García-Vidal, L. Martín-Moreno, T. Ebbesen, and L. Kuipers, *Rev. Mod. Phys.* **82**, 729 (2010).
- [3] C. L. C. Smith, N. Stenger, A. Kristensen, N. A. Mortensen, and S. I. Bozhevolnyi, *Nanoscale* **7**, 9355 (2015).
- [4] T. Søndergaard, S. Novikov, T. Holmgaard, R. Eriksen, J. Beermann, Z. Han, K. Pedersen, and S. I. Bozhevolnyi, *Nat. Commun.* **3**, 969 (2012).
- [5] E. J. H. Skjølstrup and T. Søndergaard, *J. Opt. Soc. Am B* **34**, 673 (2017).
- [6] M. Odgaard, M. G. Laursen, and T. Søndergaard, *J. Opt. Soc. Am. B* **31**, 1853 (2014).
- [7] T. Søndergaard and S. I. Bozhevolnyi, *Phys. Status Solidi B* **245**, 9 (2008).
- [8] P. Berini, *Adv. Opt. Photonics* **1**, 484 (2009).
- [9] D. Sarid, *Phys. Rev. Lett.* **47**, 1927 (1981).
- [10] A. Drezet, A. Hohenau, D. Koller, A. Stepanov, H. Ditlbacher, B. Steinberger, F. R. Aussenegg, A. Leitner, and J. R. Krenn, *Mater. Sci. Eng. B* **149**, 220 (2008).
- [11] A. Davoyan, I. Shadrivov, S. Bozhevolnyi, and Y. Kivshar, *J. Nanophotonics* **4**, 043509 (2010).
- [12] F. Liu, Y. Rao, Y. Huang, W. Zhang, and J. Peng, *Appl. Phys. Lett.* **90**, 141101 (2007).
- [13] A. Yanai and U. Levy, *Opt. Express* **17**, 14270 (2009).
- [14] H. A. Atwater and A. Polman, *Nat. Mater.* **9**, 205 (2010).
- [15] D. K. Gramotnev and S. I. Bozhevolnyi, *Nat. Mater.* **9**, 193 (2010).
- [16] M. Kuttge, F. de Abajo, and A. Polman, *Opt. Express* **17**, 10385 (2009).
- [17] P. Berini and I. D. Leon, *Nat. Photonics* **6**, 16 (2012).
- [18] N. A. Mortensen, S. Raza, M. Wubs, T. Søndergaard, and S. I. Bozhevolnyi, *Nat. Commun.* **5**, 3809 (2014).
- [19] H. Qian, Y. Xiao, and Z. Liu, *Nat. Commun.* **7**, 13153 (2016).
- [20] X. Li, A. Teng, M. Özer, J. Shen, H. Weiering, and Z. Zhang, *New J. Phys.* **16**, 065014 (2014).
- [21] W. Yan, N. A. Mortensen, and M. Wubs, *Phys. Rev. B* **88**, 155414 (2013).
- [22] R. Maniyara, D. Rodrigo, R. Yu, J. Ferrer, D. Ghosh, R. Yongsunthon, D. Baker, A. Rezikyan, F. de Abajo, and V. Pruneri, *Nature Photonics* **13**, 328 (2019).
- [23] N. D. Lang and W. Kohn, *Phys. Rev. B* **1**, 4555 (1970).
- [24] N. D. Lang and W. Kohn, *Phys. Rev. B* **3**, 1215 (1971).
- [25] W. Yan, M. Wubs, and N. A. Mortensen, *Phys. Rev. Lett.* **115**, 137403 (2015).
- [26] T. V. Teperik, P. Nordlander, J. Aizpurua, and A. G. Borisov, *Phys. Rev. Lett.* **110**, 263901 (2013).
- [27] L. Stella, P. Zhang, F. J. García-Vidal, A. Rubio, and P. García-Gonzalez, *J. Phys. Chem. C* **117**, 8941 (2013).
- [28] D. C. Marinica, A. K. Kazansky, P. Nordlander, J. Aizpurua, and A. G. Borisov, *Nano Lett.* **12**, 1333 (2012).
- [29] O. M. Bakr, V. Amendola, C. M. Aikens, W. Wenseleers, R. Li, L. D. Negro, G. C. Schatz, and F. Stellacci, *Angew. Chem.* **48**, 5921 (2009).
- [30] M. Zhu, C. M. Aikens, F. J. Hollander, G. C. Schatz, and R. Jin, *J. Am. Chem. Soc.* **130**, 5883 (2008).
- [31] R. Zhang, L. Bursi, J. Cox, Y. Cui, C. Krauter, A. Alabastri, A. Manjavacas, A. Calzolari, S. Corni, E. Molinari, E. Carter, F. de Abajo, H. Zhang, and P. Nordlander, *ACS Nano* **11**, 7321 (2017).
- [32] G. Maroulis, *J. Chem. Phys.* **121**, 10519 (2004).
- [33] J. Zuloaga, E. Prodan, and P. Nordlander, *Nano Lett.* **9**, 887 (2009).
- [34] H. Zhang, V. Kulkarni, E. Prodan, P. Nordlander, and A. O. Govorov, *J. Phys. Chem. C* **118**, 16035 (2014).
- [35] C. David and F. de Abajo, *ACS Nano* **8**, 9558 (2014).
- [36] W. Yan, *Phys. Rev. B* **91**, 115416 (2015).
- [37] S. L. Adler, *Phys. Rev.* **126**, 413 (1962).
- [38] N. Wisner, *Phys. Rev.* **129**, 62 (1963).
- [39] J. K. Lindhard, *Dan. Vidensk. Selsk. Mat. Fys. Medd.* **28**, 8 (1954).
- [40] N. D. Mermin, *Phys. Rev. B* **1**, 2362 (1970).
- [41] P. J. Feibelman, *Phys. Rev. B* **12**, 1319 (1975).
- [42] P. J. Feibelman, *Prog. Surf. Sci.* **12**, 287 (1982).
- [43] O. Keller, *Phys. Rev. B* **33**, 990 (1986).
- [44] J. Kohanoff, *Electronic Structure Calculations for Solids and Molecules: Theory and Computational Methods*, 1st ed. (Cambridge University Press, Cambridge, 2006).
- [45] W. Zhu, R. Esteban, A. G. Borisov, J. J. Baumberg, P. Nordlander, H. J. Lezec, J. Aizpurua, and K. B. Crozier, *Nat. Commun.* **7**, 11495 (2016).
- [46] F. de Abajo, *J. Phys. Chem. C* **112**, 17983 (2008).
- [47] S. Raza, G. Toscano, A. Jauho, M. Wubs, and N. A. Mortensen, *Phys. Rev. B* **84**, 121412(R) (2011).
- [48] K. J. Savage, M. M. Hawkeye, R. Esteban, A. G. Borisov, J. Aizpurua, and J. J. Baumberg, *Nature (London)* **491**, 574 (2012).
- [49] S. Laref, J. Cao, A. Asaduzzaman, K. Runge, P. Deymier, R. Ziolkowski, M. Miyawaki, and K. Muralidharan, *Opt. Express* **21**, 11827 (2013).
- [50] L. Novotny and B. Hecht, *Principles of Nano-Optics*, 2nd ed. (Cambridge University Press, Cambridge, 2012).
- [51] P. B. Johnson and R. W. Christy, *Phys. Rev. B* **6**, 4370 (1972).
- [52] T. Søndergaard, *Green's Function Integral Equation Methods in Nano-Optics*, 1st ed. (CRC Press, Boca Raton, FL, 2019).
- [53] P. Simesen, T. Søndergaard, E. Skovsen, J. Fiutowski, H. Rubahn, S. I. Bozhevolnyi, and K. Pedersen, *Opt. Express* **23**, 16356 (2015).
- [54] S. Ramos, H. Farooq, H. Alghasam, A. Bernussi, and L. Peralta, *Opt. Express* **26**, 19718 (2018).
- [55] M. V. Klein and T. E. Furtak, *Optics*, 2nd ed. (Wiley, New York, 1986).
- [56] Z. F. Öztürk *et al.*, *J. Nanophotonics* **5**, 051602 (2011).
- [57] S. Boriskina, T. Cooper, L. Zeng, G. Ni, J. Tong, Y. Tsurimaki, Y. Huang, L. Meroueh, G. Mahan, and G. Chen, *Adv. Opt. Photonics* **9**, 775 (2017).
- [58] J. Khurgin, *Nat. Nanotechnol.* **10**, 2 (2015).
- [59] R. Zia, M. D. Selker, and M. L. Brongersma, *Phys. Rev. B* **71**, 165431 (2005).
- [60] B. Lambrecht, J. Krenn, G. Schider, H. Ditlbacher, M. Salerno, N. Felidj, A. Leitner, F. Aussenegg, and J. Weeber, *Appl. Phys. Lett.* **79**, 51 (2001).
- [61] J. W. Petefish and A. C. Hillier, *Anal. Chem.* **86**, 2610 (2014).
- [62] W. Knoll, *Annu. Rev. Phys. Chem.* **49**, 569 (1998).
- [63] J. P. Perdew and A. Zunger, *Phys. Rev. B* **23**, 5048 (1981).
- [64] V. Eyert, *J. Comput. Phys.* **124**, 271 (1996).
- [65] R. Petersen, T. G. Pedersen, M. N. Gjerding, and K. S. Thygesen, *Phys. Rev. B* **94**, 035128 (2016).

*Correction:* The article identification number was incorrect in Ref. [1] and has been fixed, enabling access to the online article.